Modelling of the Frequency Response to Dynamic Nanoindentation of Soft Hydrated Anisotropic Materials: Application to Articular Cartilage

Taffetani M.[1], Bertarelli E.[1,2], Gottardi R.[3,4], Raiteri R.[5] and Vena P.[1,2]

Abstract: Dynamic nanoindentation is a novel nanomechanical testing that is being increasingly used to characterize the frequency response of viscoelastic materials and of soft hydrated biological tissues at the micrometric and nanometric length scales. This technique is able to provide more information than those obtained by simple indentation; however, its interpretation is still an open issue for complex materials such as the case of anisotropic biological tissues that generally have a high water content. This work presents a numerical model to characterize the frequency response of poro-elastic tissues subjected to harmonic indentation loading with particular regard to the effect of geometrical characteristic lengths (i.e. penetration depth and indenter radius) and to the effect of tissue anisotropy. The analysis is performed by a frequency domain finite element axi-symmetric model of harmonic spherical indentation. Under the basic hypotheses of poro-elastic response of the material and of strain-independent isotropic permeability, this work shows that anisotropic properties of the tissue can be obtained from one single dynamic indentation experiment. In particular, we show that anisotropy of the tissue is a necessary property to correctly predict the experimental frequency response in terms of drained to undrained ratio and of tangent of phase lag.

Keywords: dynamic nanoindentation, poroelasticity, soft-hydrated tissues, finite elements.

---

[1] Department of StructuralEngineerng, Politecnico di Milano, Piazza Leonardo da Vinci, 32 20133 Milano, Italy

[2] IRCCS, IRCCS, Istituto Ortopedico Galeazzi, Milano Italy

[3] Department of Orthopaedic Surgery, University of Pittsburgh, Pittsburgh, USA

[4] Fondazione Ri.MED, Palermo, Italy

[5] Department of Biophysical and Electronic Engineering, University of Genova, Genova, Italy

1 Introduction

Nowadays, the mechanical characterization of tissues and other biological materials is of paramount relevance in both clinical medicine and biomaterials science [Ebenstein and Pruitt (2006)]. In this direction, an insight on material properties and their links with probing technique length scale and time scale is topical. In this paper the articular cartilage (AC) is considered as a paradigm of a complex tissue with mechanical functions.

From a structural viewpoint, AC can be seen as a solid porous matrix saturated with water that can flow through pores; the solid matrix consists mainly of type II collagen containing fibrils and negative charged proteoglycans, forming the extracellular matrix, as well as of a small cellular component (chondrocytes) [Buckwalter and Mankin (1997);Wilson, van Donkelaar, van Rietbergen and Huiskes (2007)].

From a mechanical viewpoint, articular cartilage is a complex structure, both inhomogeneous and anisotropic, which exhibits a time-dependent mechanical behavior. Its anisotropic mechanical properties are such that its mechanical response varies with tissue orientation with respect to tissue loading: collagen fibrils' orientation is mainly parallel to the articular surface in the superficial zone and varies with depth, becoming perpendicular to surface in the deep zone [Huang, Stankiewicz, Athesian and Mow (2005)].

The time dependent behaviour is due to two main mechanisms: i) viscoelasticity which is intrinsically dependent on the molecular structure and, ii) poroelasticity which is an extrinsic mechanisms related to the the flow of fluid through pores [Hu, Zhao, Vlassak and Suo (2010)]. Macro-scale experiments including confined/unconfined compression and indentation [Armstrong, Lai, and Mow (1984); Korhonen, Laasanen, Toyras, Rieppo, Hirvonen, Helminen and Jurvelin (2002)], tension [Kempson, Muir, Pollard and Tuke (1973)], shear [Spirt, Mak and Wassel (1989)] have been used to characterize the time dependent behaviour of the tissue.

Recently, it has been reported that macro-scale mechanics of collagen-based tissues does not follow directly from the mechanics of the individual fibrils, while the tissue's response strongly depends on the arrangement of the fibrils at the micro-scale [Fratzl (2008), Chandran and Barocas (2006), Tang, Buehler, Moran (2009), Maceri, Marino, Vairo(2010)]. As a consequence, cartilage can be considered a great example to motivate studies on different experimental techniques able to probe different characteristic sizes and time scales.

This work deals with the frequency response of this soft anisotropic hydrated tissue subject to spherical dynamic nanoindentation. This experimental technique represents an effective tool which is capable of probing local gradients and heterogeneities, as well as to drive diverse deformation modes by changing inden-

ter tip geometry, loading conditions and experimental time scale [Oyen and Cook (2009)]. Nanoindentation is widely used also for its intrinsic experimental simplicity in terms of sample preparation [Gouldstone, Chollacoop, Dao, Li, Minor and Shen (2007)]. Frequency domain analyses coupled with nanoindentation has been shown to have a potential to characterize articular cartilage; by exploiting this technique, in the work of Han [Han, Frank, Greene, Lee, Hung, Grodzinsky and Ortiz (2011)] fluid flow induced poroelasticity was shown to primarily govern the frequency dependent energy dissipation, while longer time scale force relaxation mainly reflects viscoelasticity.

However, relating the response of indentation to mechanical properties is still a challenge for fluid filled tissues or materials; under these circumstances, the response is both time dependent and size dependent. For an indentation process involving length scales by far larger than the constituents size, the viscoelastic relaxation time is found to be independent on the contact size. On the contrary, the poroelastic relaxation time is quadratic in the contact size [Hu, Zhao, Vlassak and Suo (2010)].

The effect of geometrical aspects in material response have been emphasized by several authors, especially in the time domain: Simha [Simha, Jin, Hall, Chiravarambath and Lewis (2007)] showed the effect of the end diameter of flat-ended conical and cylindrical tips on equilibrium modulus; Lu [Lu, Wan, Guo and Mow (2010)] studied the effect of aspect ratio on several parameters in creep tests; in the work by Hu [Hu, Zhao, Vlassak and Suo (2010)] dimensionless relaxation functions for different geometries of the indenter tip were extracted.

The work of Han [Han, Frank, Greene, Lee, Hung, Grodzinsky and Ortiz (2011)] shows the difference between the characteristic poroelastic relaxation time and the viscoelastic behavior, by relating them to the nanostructure of cartilage. This fundamental consideration allows differentiation of these two mechanical behaviors using indentation. This highlights the need for models to interpret the experimental results of instrumented indentation on soft tissues and gels exhibiting a poroelastic or poro-viscoelastic mechanical response. To this aim, the recent work of Hu [Hu, Chen, Whitesides, Vlassak and Suo (2011)] shows a method based on indentation to characterize an elastomeric gel.

While viscoelasticity has been widely studied and closed form solutions for the analysis and interpretation of indentation data are available (e.g[Vandamme and Ulm (2006)]), the interpretation of poroelastic materials response under indentation is still an open issue. Poroelastic theories were first developed and used for the analysis of wet soils and later applied to the study of soft tissues: the early works dealt with quasi-static and dynamic loading of both linear isotropic and anisotropic materials undergoing infinitesimal strain [Biot (1941)]; recent works take into con-

sideration also finite strain and nonlinearity [Simon (1992)] or full dynamic formulations [Karpfinger, Muller and Gurevich (2009)].

Two different equivalent approaches can be used for the analysis of a soft hydrated tissue: the mixture model and the poroelastic model. In the former, the primary variables are related to the different species that compose such material: as an example, in the work of Mow [Mow, Kuei, Lai and Armstrong (1980)] the biphasic mixture model considers the solid phase displacement, u, and the fluid phase displacement, U, ('u-U' model) as variables, while in the work of Lu [Lu, Wan, Guo and Mow (2010)] the triphasic mixture model introduces also the effect of negative charged proteoglycans on fluid pressure. Moreover, in [Almeida and Spilker (1998)] the biphasic model has been extended to account for transversely isotropy of cartilage in a finite element setting. In the latter, the primary variables are the solid phase displacement, u, and the relative displacement between solid and fluid phases, w, ('u-w' model) or the pore pressure, π ('u-π' model).

In the poroelastic approach, the fluid filled tissue is viewed as a composite material with fluid and solid phases which fill the space in a homogeneous manner.

The aim of the present work is to study, by means of numerical models, the frequency response of soft hydrated tissues to dynamic indentation with specific regard to the effects of material anisotropy and characteristic size of the experiment. It will be shown that anisotropic properties and tissue permeability affect the dynamic response to dynamic indentation in a peculiar fashion along with the geometric features of the test.

To achieve our goal, a suitably developed computational model for the simulation of harmonic forced oscillation of poroelastic media in the frequency domain is used. The analytical solution available for confined compression tests are used as benchmark. The computational model is proven to be well suited to explore the effects of material constitutive parameters and of the characteristic size in harmonic nanoindentation tests. Sensitivity analyses are performed for both geometrical and constitutive parameters. In the former case, a linear poroelastic isotropic material of given Young's modulus, Poisson's ratio and permeability is indented using a spherical tip. The role played by the indenter radius and the indenter penetration depth are highlighted. In the latter case study, a linear elastic transversely isotropic material is indented in a fixed geometric configuration, by varying the anisotropy ratio and the 'out of plane' Poisson's ratio.

2   Problem formulation

In this section the problem formulation for a fully saturated porous medium in spatial configuration is briefly introduced. Under this condition, no air or gas phases

are accounted for.

According to [Cowin and Doty (2006)], if one considers a representative volume element (RVE) subjected to a total stress $\boldsymbol{\sigma}$ and to a pressure p, the deformation of the medium can be split in two parts (Voigt notation is adopted):

(i) i) Elastic deformation of the solid matrix due to the effective stress $\boldsymbol{\sigma}'$ [Terzaghi (1943)] namely

$$\boldsymbol{\sigma}' = \boldsymbol{\sigma} + \mathbf{m}p \tag{1}$$

where $\boldsymbol{\sigma}$ is the total Cauchy stress, $\mathbf{m} = [1\ 1\ 1\ 0\ 0\ 0]$.

(ii) ii) Volumetric elastic deformation due to the fluid pressure.
By combining the above two contributions, the total deformation can be written as

$$\boldsymbol{\varepsilon} = \mathbf{C^d}^{-1}(\boldsymbol{\sigma} + \mathbf{m}p) - \mathbf{m}\frac{p}{3K_s} \tag{2}$$

where $\mathbf{C^d}$ is the elastic drained stiffness matrix, K_s is the bulk modulus of the solid matrix. Then, the total stress is

$$\boldsymbol{\sigma} + \alpha\mathbf{m}p = \mathbf{C^d}\boldsymbol{\varepsilon} \tag{3}$$

where $\alpha = 1 - \frac{\mathbf{m}^T\mathbf{C^d}\mathbf{m}}{9K_s}$ is the Biot coefficient. In case of isotropic material, the drained bulk modulus K_T is defined as $K_T = \frac{\mathbf{m}^T\mathbf{C^d}\mathbf{m}}{9} = \frac{3\mathbf{C^d}}{9(1-2v)}$ in which v is the Poisson's ratio and $\alpha = 1 - \frac{K_T}{K_s}$. In this way, using two mechanical parameters as K_s and K_T, the parameter α is defined.

Concerning the fluid phase, the total variation of fluid content $\dot{\zeta}$ has to be defined. Its time variation is due to several contributions:

- Total macroscopic deformation of the structure;

- Fluid compression due to pressure increment;

- Matrix compression due to pressure increment;

- Matrix deformation due to matrix stresses.

Introducing the porosity a as the ratio between the volume of pore fluid and the total volume, $a = \frac{dV^v}{dV}$, the total variation of fluid can be written as

$$\dot{\zeta} = \mathbf{m}^T\dot{\boldsymbol{\varepsilon}} + n\frac{\dot{p}}{K_F} + (1-n)\frac{\dot{p}}{K_S} - \frac{\mathbf{m}^T\dot{\boldsymbol{\sigma}}'}{3K_S} \tag{4}$$

that can be reduced as

$$\dot{\zeta} = \alpha \mathbf{m}^T \dot{\boldsymbol{\varepsilon}} + \frac{\dot{p}}{M_B} \tag{5}$$

where the Biot modulus M_B is defined as $\frac{1}{M_B} = \frac{n}{K_F} + \frac{\alpha - n}{K_S}$, K_F is the bulk modulus of fluid phase and the dots indicates the partial derivative with respect to time.

Equations (3) and (5) describe the coupled constitutive equations for a poroelastic medium:

$$\begin{cases} \boldsymbol{\sigma} + \alpha \mathbf{m} p = \mathbf{C}^{\mathbf{d}} \boldsymbol{\varepsilon} \\ \dot{\zeta} = \alpha \mathbf{m}^T \dot{\boldsymbol{\varepsilon}} + \frac{\dot{p}}{M_B} \end{cases} \tag{6}$$

The system of equations (6) holds for small displacements and small strains when hydrostatic fluid stresses, isothermal process and total fluid saturation are assumed. Since bulk modulus of the solid matrix is much larger than volumetric compressibility of the porous medium, the assumption of intrinsic incompressibility is done. If also fluid is assumed incompressible, the Biot coefficient and the Biot modulus become, respectively, $\alpha = 1$ and $\frac{1}{M_B} = 0$ [Simon (1992)].

The equilibrium equation, in a general framework, is

$$\begin{cases} div(\boldsymbol{\sigma}) = \mathbf{F} + \rho \ddot{\mathbf{u}} & in \ \Omega \\ \boldsymbol{\sigma} \mathbf{n} = \mathbf{f} & in \ \Gamma \end{cases} \tag{7}$$

where $\mathbf{F}$ and $\mathbf{f}$ are, respectively, body forces and surface forces in a RVE of volume Ω and boundary Γ.

In the absence of inertia and body forces, the terms $\mathbf{F}$ and $\rho \ddot{\mathbf{u}}$ are equal to zero.

The flow of the pore fluid is assumed to obey Darcy's law, i.e. the fluid flux J is proportional to the gradient of the pressure p:

$$\mathbf{J} = -\mathbf{K} \nabla p \tag{8}$$

where $\mathbf{K} \left[\frac{m^4}{N*s} \right]$ is the permeability tensor. In case of isotropy and homogeneity, the permeability reduces to a scalar k which can be a function of the void ratio, a.

The continuity equation is

$$-div(J) = \dot{\zeta} \tag{9}$$

Substituting the expression (8) in (5), under the hypothesis of isotropic and homogeneous permeability, the continuity equation becomes

$$kdiv(\nabla p) = \alpha \mathbf{m}^T \dot{\boldsymbol{\varepsilon}} \tag{10}$$

The governing equations are discretized by using a Galërkin approach leading to the following system of linear equations in the matrix form (i is the imaginary unit):

$$\begin{cases} \mathbf{K}_{uu}\mathbf{U}_{node}e^{ift} - \mathbf{G}_{up}\mathbf{P}_{node}e^{ift} = \mathbf{F}_u e^{ift} \\ if\mathbf{G}_{pu}\mathbf{U}_{node}e^{ift} + \mathbf{K}_{pp}\mathbf{P}_{node}e^{ift} = \mathbf{F}_p e^{ift} \end{cases} \tag{11}$$

with

$$\mathbf{K}_{uu}{}^T = \sum_e \mathbf{L}_u^{eT} \int_{\Omega_e} \mathbf{B}_u{}^T \mathbf{C}^{\mathbf{d}} \mathbf{B}_u d\Omega \mathbf{L}_u^e, \quad \mathbf{G}_{up}{}^T = \sum_e \mathbf{L}_p^{eT} \int_{\Omega_e} \mathbf{N}_p{}^T \mathbf{m}^T \mathbf{B}_u d\Omega \mathbf{L}_u^e,$$

$$\mathbf{G}_{pu}{}^T = \sum_e \mathbf{L}_u^{eT} \int_{\Omega_e} \mathbf{B}_u{}^T \mathbf{m}^T \mathbf{N}_p d\Omega \mathbf{L}_p^e, \quad \mathbf{K}_{pp}{}^T = \sum_e \mathbf{L}_p^{eT} \int_{\Omega_e} \mathbf{B}_p{}^T k \mathbf{B}_p d\Omega \mathbf{L}_p^e$$

in which the **L** matrices are connectivities, the **N** matrices are shape functions and **B** matrices represent compatibility between strain and displacements.

The above discretized system has been formulated disregarding inertial and body forces effects.

The system of linear equations (11) has been obtained by imposing a harmonic forced displacement $\overline{\mathbf{U}}$ at a given frequency f and known magnitude $\mathbf{U}_0$

$$\overline{\mathbf{U}} = \mathbf{U}_0 e^{ift} \tag{12}$$

and a model response of the form:

$$\begin{cases} \mathbf{U} = \mathbf{U}_{node}e^{ift} \\ \mathbf{P} = \mathbf{P}_{node}e^{ift} \end{cases} \tag{13}$$

where $\mathbf{U}_{node}$ and $\mathbf{P}_{node}$ are, in general, complex numbers, defined by a modulus and a phase shift.

Finally, the poroelastic problem under harmonic forced displacement (in the case of imposed force, the derivation is similar) becomes, in matrix form

$$\begin{bmatrix} \mathbf{K}_{uu} & -\mathbf{G}_{up} \\ if\mathbf{G}_{pu} & -\mathbf{K}_{pp} \end{bmatrix} * \begin{bmatrix} \mathbf{U}_{node} \\ \mathbf{P}_{node} \end{bmatrix} = \begin{bmatrix} \mathbf{F}_u \\ \mathbf{F}_p \end{bmatrix} \tag{14}$$

The above set of finite element equations have been implemented in the MATLAB environment.

2.1   Limit cases: the drained and the undrained states

As mentioned above, the behavior of a poroelastic medium is governed by the mechanical properties of the matrix and the flow of the fluid through pores; these two aspects can be analyzed separately by studying the frequency response for two limit cases.

In particular, if one considers the limit to quasi static loading ($f \rightarrow 0$), the fluid pressure is uniform into the specimen and there is equilibrium with the external pressure: the behavior is then governed by the porous matrix only; this condition is defined as drained state. The second limit case is the ideal step loading ($f \rightarrow \infty$), in which $\dot{\zeta}=0$ and the hydrostatic stress component is carried by the fluid: this condition is defined as undrained state. It should be borne in mind that the proposed boundary conditions are ideal situations that are seldom found in laboratory experiments. In particular, while the drained condition can be well approximated by applying quasi-static loading or by waiting for poroelastic equilibrium, the undrained condition is seldom achieved in harmonic loading since dynamic effects introduced by inertial properties of the experimental set-up will affect the high frequency behavior. Nevertheless, undrained condition is of interests for a comprehensive description of the time dependent behavior of poroelastic fully saturated media.

2.2   Limit cases: theoretical model

In the framework of classical linear elastic contact mechanics solution, the relation between the applied force and the displacement registered for a rigid indenter of axi-symmetric shape can be described as [Shahsavari and Ulm (2009)]:

$$F = \Phi M H^{(1+1/q)} \tag{15}$$

where Φ accounts for the indenter specific geometry, q is the degree of the homogeneous function related to geometry and M is the indentation modulus. If the indenter tip is a sphere or a cone, equation (15) becomes, respectively

$$F = \frac{4}{3} M \sqrt[2]{R} H^{3/2} \tag{16a}$$

$$F = \frac{4}{\pi} M tan\theta H^2 \tag{16b}$$

where θ is the half-cone angle.

According to [Delafargue and Ulm (2009)], in the case of axi-symmetric tip, it is possible to relate the indentation modulus to the elastic properties of the material. Recalling C_{ijhk} the generic entry of the fourth order stiffness tensor, one can obtain

$$M = \frac{C_{1111}^2 - C_{1122}^2}{C_{1111}} \tag{17a}$$

$$M = 2 \sqrt[2]{\frac{C_{1111}C_{3333} - C_{1133}^2}{C_{1111}} \left(\frac{1}{C_{1313}} + \frac{2}{\sqrt[2]{C_{1111}C_{3333}} + C_{1133}} \right)} \tag{17b}$$

Equation (17.a) refers to isotropic materials; whereas, equation (17.b) refers to transversely isotropic materials in which the directions 1 and 2 define the plane of isotropy and direction 3 is the loading direction. Equations (17.a,b) are obtained for conical indenter; Vlassak [Vlassak, Ciavarella, Barber and Wang (2003)] reports that both conical and spherical indentation theories extract the same value for the indentation modulus M.

For a poroelastic material, the information on the drained state is contained in the elastic stiffness tensor in drained condition $\mathbf{C^d}$; calling $\mathbf{S^d} = \mathbf{C^{d\,-1}}$ the elastic compliance tensor in the drained state, it is possible to derive the compliance tensors in the undrained condition, as proposed by [Cowin and Doty (2006)]

$$\mathbf{S^u} = \mathbf{S^d} - K \left(\mathbf{S^d m} \times \mathbf{S^d m} \right) \tag{18}$$

where $K = \left(\mathbf{m^T S^d m} \right)^{-1}$.

Then, if one applies the Equation (17.a) or (17.b) using $\mathbf{C^d}$ and $\mathbf{C^u}$, defining the elastic stiffness tensor in undrained condition as $\mathbf{C^u} = \mathbf{S^{u\,-1}}$, it is possible to obtain the values of M, in both drained and undrained conditions.

2.3 Limit cases: numerical model

Since vectors $\mathbf{U}_{node}$ and $\mathbf{P}_{node}$ have complex entries, they can be explicitly expressed as

$$\begin{cases} \mathbf{U}_{node} = \mathbf{U}_r + i\mathbf{U}_i \\ \mathbf{P}_{node} = \mathbf{P}_r + i\mathbf{P}_i \end{cases} \tag{19}$$

where $\mathbf{U}_r$ and $\mathbf{P}_r$ are the real parts and $\mathbf{U}_i$ and $\mathbf{P}_i$ are the imaginary parts.

Substituting (19) in (11), the problem can be written as

$$\begin{cases} \mathbf{K}_{uu}(\mathbf{U}_r + i\mathbf{U}_i) - \mathbf{G}_{up}(\mathbf{P}_r + i\mathbf{P}_i) = \mathbf{F}_{ur} \\ if\mathbf{G}_{pu}(\mathbf{U}_r + i\mathbf{U}_i) - \mathbf{K}_{pp}(\mathbf{P}_r + i\mathbf{P}_i) = \mathbf{F}_{pi} \end{cases} \tag{20}$$

And, simplifying,

$$\begin{cases} \mathbf{K}_{uu}\mathbf{U}_r + i\mathbf{K}_{uu}\mathbf{U}_i - \mathbf{G}_{up}\mathbf{P}_r - i\mathbf{G}_{up}\mathbf{P}_i = \mathbf{F}_{ur} \\ if\mathbf{G}_{pu}\mathbf{U}_r - f\mathbf{G}_{pu}{}^T\mathbf{U}_i - \mathbf{K}_{pp}\mathbf{P}_r - i\mathbf{K}_{pp}\mathbf{P}_i = \mathbf{F}_{pi} \end{cases} \tag{21}$$

This system of two vector equations can be split in the real and imaginary parts giving a system of four vector equations:

$$
\begin{cases}
\mathbf{K}_{uu}\mathbf{U}_r - \mathbf{G}_{up}\mathbf{P}_r = \mathbf{F}_{ur} \\
\mathbf{K}_{uu}\mathbf{U}_i - \mathbf{G}_{up}\mathbf{P}_i = 0 \\
f\mathbf{G}_{pu}\mathbf{U}_i + \mathbf{K}_{pp}\mathbf{P}_r = 0 \\
f\mathbf{G}_{pu}\mathbf{U}_r - \mathbf{K}_{pp}\mathbf{P}_i = \mathbf{F}_{pi}
\end{cases}
\tag{22}
$$

If $f \to 0$ (drained state), the system (22) becomes

$$
\begin{cases}
\mathbf{K}_{uu}\mathbf{U}_r - \mathbf{G}_{up}\mathbf{P}_r = \mathbf{F}_{ur} \\
\mathbf{K}_{uu}\mathbf{U}_i - \mathbf{G}_{up}\mathbf{P}_i = 0 \\
\mathbf{K}_{pp}\mathbf{P}_r = 0 \\
\mathbf{K}_{pp}\mathbf{P}_i = \mathbf{F}_{pi}
\end{cases}
\tag{23}
$$

and the solution, in terms of pressure and displacement, is

$$
\begin{cases}
\mathbf{U}_r = \mathbf{K}_{uu}^{-1}\mathbf{F}_{ur} \\
\mathbf{U}_i = \mathbf{K}_{uu}^{-1}\mathbf{G}_{up}\mathbf{K}_{pp}^{-1}\mathbf{F}_{pi} \\
\mathbf{P}_r = 0 \\
\mathbf{P}_i = \mathbf{K}_{pp}^{-1}\mathbf{F}_{pi}
\end{cases}
\tag{24}
$$

If $f \to \infty$ (undrained state), the system (22) becomes

$$
\begin{cases}
\mathbf{K}_{uu}\mathbf{U}_r - \mathbf{G}_{up}\mathbf{P}_r = \mathbf{F}_{ur} \\
\mathbf{K}_{uu}\mathbf{U}_i - \mathbf{G}_{up}\mathbf{P}_i = 0 \\
\mathbf{G}_{pu}\mathbf{U}_i = 0 \\
\mathbf{G}_{pu}\mathbf{U}_r = 0
\end{cases}
\tag{25}
$$

and the solution, in terms of pressure and displacement, is

$$
\begin{cases}
\mathbf{U}_r = \mathbf{K}_{uu}^{-1}\left(\mathbf{F}_{ur} + \mathbf{G}_{up}\mathbf{P}_r\right) \\
\quad = \left(\mathbf{K}_{uu}^{-1} + \mathbf{K}_{uu}^{-1}\mathbf{G}_{up}(\mathbf{G}_{pu}\mathbf{K}_{uu}^{-1}\mathbf{G}_{up})^{-1}\mathbf{G}_{pu}\mathbf{K}_{uu}^{-1}\right)\mathbf{F}_{ur} \\
\mathbf{U}_i = \mathbf{K}_{uu}^{-1}\mathbf{G}_{up}\mathbf{P}_i = 0 \\
\mathbf{P}_r = -(\mathbf{G}_{pu}\mathbf{K}_{uu}^{-1}\mathbf{G}_{up})^{-1}\mathbf{G}_{pu}\mathbf{K}_{uu}^{-1}\mathbf{F}_{ur} \\
\mathbf{P}_i = 0
\end{cases}
\tag{26}
$$

In a displacement-based test, the reaction force under the indenter is the sum of the reaction force on each node 'of the indenter'. For both $f \to 0$ and $f \to \infty$, these

nodal forces are such that

$$\begin{cases} \mathbf{F}_{ur} \neq 0 \\ \mathbf{F}_{ui} = 0 \end{cases} \tag{27}$$

This result shows that, at both bounds, the behavior can be described only by real forces and displacements.

3 Model implementation

The laboratory test is an oscillatory indentation spectroscopy carried out applying a harmonic movement of the indenting probe while sweeping the frequency, superimposed to a constant preload. This test mode is simulated through a two steps numerical simulation. In the first step, the pre-loading is applied and a static (time independent) indentation is simulated; in the second step, a harmonic loading is applied and the problem is solved in the frequency domain, on the reference (initial) configuration obtained from the pre-load indentation. A two-dimensional axi-symmetric model for spherical poroelastic dynamic indentation has been built. A rigid, spherical indenter of radius R is pressed into a cylindrical sample of radius W and height B. Indentation depth is denoted by H. The radius of the specimens is 20 times larger than the radius of the tip and the height of the specimen is 30 times larger than the indentation depth. These conditions are assumed to guarantee that the mechanical response to indentation is not affected by the domain boundaries.

As a first step, model geometry is defined and discretization is performed (approximately 15000 first order four-node elements) using the commercial displacement-based finite element code Abaqus 6.8-EF1 (Simulia, Providence, RI, USA). A quasi-static indentation is simulated with depth H to obtain the deformed state to be used as input for the harmonic loading. According to the purpose of this step, the material model is linear elastic. The contact radius is resolved with approximately 30 elements.

Subsequently, the deformed geometry is used as input for the frequency domain model developed within the Matlab environment (MathWorks, Natick, MA, USA). The deformed mesh is used as stress-free initial configuration for the simulation of the dynamic nanoindentation in the frequency domain, according to the poroelastic framework introduced in section 2. A poroelastic material is now considered. A harmonic vertical displacement of 0.1mm is imposed to the node set representing the contact radius. It is worth noting that for the linearized framework (small displacement oscillations) implemented in this work, the model response is independent of the displacement oscillation magnitude. The investigated range of frequencies varies from 0 Hz (drained condition) up to the undrained condition, here simulated with a conventional frequency of 10^7 Hz.
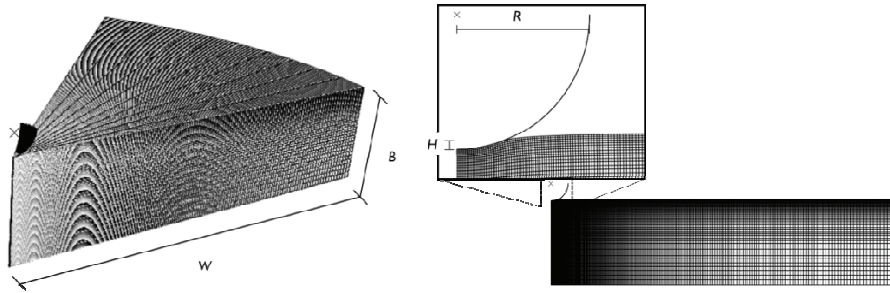
Figure 1: (a) a 3D visualization of the axisymmetric mesh in the undeformed configuration (left) and (b) the 2D axisymmetric mesh of the model in the deformed configuration with a zoom of the zone under the tip. The generic dimensions are highlighted.

The output of the dynamic simulations is then the vertical reaction force on the indenter tip for each imposed frequency f. Reduced storage modulus E'^* and reduced loss modulus E''^* are calculated according to the expressions [Cheng, Ni and Cheng (2006)]

$$
\begin{aligned}
E'^*(f) &= \tfrac{1}{2}\tfrac{1}{\sqrt[2]{RH}}\left|\tfrac{\triangle P(f)}{\triangle H}\right|\cos\phi(\phi_f) \\
E''^*(f) &= \tfrac{1}{2}\tfrac{1}{\sqrt[2]{RH}}\left|\tfrac{\triangle P(f)}{\triangle H}\right|\sin(\phi_f)
\end{aligned}
\tag{28}
$$

in which $\triangle P(f)$ is the amplitude of the harmonic force output, $\triangle H$ is the forced displacement input and ϕ_f is the phase shift between input and output; R and H are the tip radius and the indentation depth.

The effect of the constitutive parameters is analyzed through the following quantities:

- the normalized storage modulus (it recalls the consolidation rate defined in time domain problems), defined as follows,

$$
\overline{E'^*} = \frac{(E'^*(f)-E'^*(0))}{(E'^*(f\to\infty)-E'^*(0))}
\tag{29}
$$

which highlights the effect of geometric parameters;

- the drained to undrained ratio $\frac{E'^*(0)}{E'^*(f\to\infty)}$ which is dependent on the tissue properties and independent of its time response;

- the value of the tangent of the phase shift, $tan(\phi_f)$, versus frequency that explains how the porosity affects the behavior of the poroelastic medium. This is a measure of the balance between conservative and dissipative contributions: the higher the tangent, the more relevant is the effect of porosity. The peak frequency, f_{max}, can be regarded as a measure of the typical time scale in which fluid flow mainly occurs;

- numerical results will also be analyzed by using the normalized frequency defined in analogy to [Galli and Oyen (2009)] as follows:

$$\overline{f} = f \frac{RH}{m} \tag{30}$$

where the parameter m is proportional to the permeability and to the elastic modulus; m is kept constant through all the simulations performed.

4 Results

The validation of the numerical code in the frequency domain is carried out by solving the plane strain problem of confined compression for which the analytical solution is known. The bottom and the lateral edges are impermeable whereas the top boundary is permeable. Due to the homogeneity along the horizontal direction (x direction), the problem can be simply reduced to a 1-D problem. In particular, the analytical solution in terms of fluid pressure and of top boundary displacement reads [Cowin and Doty (2006)]:

$$p(z,t) = P_0(1 + tan\left(\sqrt{\frac{ifL^2}{c}}\right) sinh\left(\frac{z}{L}\sqrt{\frac{ifL^2}{c}}\right) - cos\left(\frac{z}{L}\sqrt{\frac{ifL^2}{c}}\right))e^{ift} \tag{31a}$$

$$u(0,t) = \frac{1}{E}\sqrt{\frac{c}{ifL^2}}tan\left(\sqrt{\frac{ifL^2}{c}}\right)e^{ift} \tag{31b}$$

where f is the frequency and c is a material parameter. In case of isotropic elasticity and incompressible materials, $c = \frac{kE(1-v^d)}{(1+v^d)(1-2v^d)}$ in which E [MPa] is the Young's Modulus, v^d is the drained Poisson's ratio, k [$\frac{m^2 N}{s}$] is the permeability. Equation (31.a) shows the value of the pressure as a function of the depth of the specimen and of the frequency, while equation (31.b) shows the value of the displacement of the upper surface as a function of the frequency. The implemented model well compares with the reference analytical solution: Figure 2 shows the fluid pressure distribution across the normalized thickness for a selected frequency.
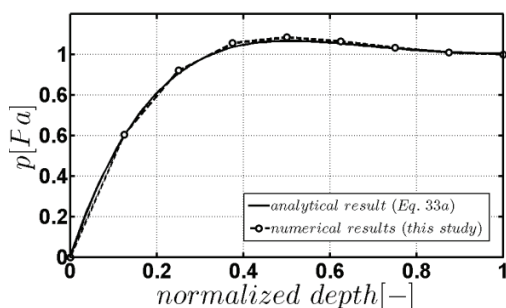
Figure 2: Pressure versus normalized depth for the 1-D benchmark problem; symbols refer to the finite element formulation; the solid line refers to the analytical solution [Cowin and Doty (2006)].

4.1   Effect of geometrical parameters

The harmonic indentation problem is first studied with respect to geometrical parameters. The indented material is modeled at this stage as homogeneous, isotropic and linear elastic with Young's modulus $E_i = 300 \; KPa$, Poisson's ratio $\nu_i = 0.22$ and constant permeability $k_i = 10^{-15} \frac{m^4}{N \, s}$. These values fall within the range of interest for AC tissue. Indeed, in the literature, a wide range of values for the drained Young's modulus can be found. Variability is basically a consequence of the specific type of tissue (human or animal or site of harvesting) as well as the probing technique. Jurvelin [Jurvelin, Buschmann and Hunziker (2003)] report Young's modulus of 581 ± 168 kPa after unconfined compression on samples extracted from the patellofemoral groove of human knee; Boschetti [Boschetti, Pennati, Gervaso, Peretti and Dubini (2004)] performs unconfined compression tests on hip human native cartilage, obtaining 250 ± 150 kPa on the surface, 350 ± 100 on the middle and 500 ± 200 kPa on deep layers. Kiviranta [Kiviranta, Lammentausta, Töyräs, Kiviranta and Jurvelin (2008)] carries out indentation on human patellae cartilage at different stages of tissue degradation due to osteoarthritis, that yielded values of 640 ± 300 kPa for healthy cartilage, 700 ± 620 kPa for early degeneration, down to 210 ± 260 kPa for advanced degradation. Concerning animal samples, Miller and Morgan (2010) recently report from microindentation and unconfined compression on human knee patellofemoral groove samples a mean value for Young's modulus of 740 kPa.

Different indentation depths and indentation radii are considered and the results for the different cases are compared. In particular, Table 1.a summarizes the (R,H) sets along with model geometries used here to evaluate the effect of indentation depth

while indenter radius R is kept constant. Table 1.b reports the (R,H) sets and the respective specimen geometries adopted to investigate the effect of indenter/specimen size (i.e., the characteristic size), while the H/R ratio (i.e., the equivalent deformation) is kept constant.

Table 1 (a): (R,H) case studies and respective model geometries for the evaluation of indentation depth effect (constant indenter radius). Sample radius W set to 20 times the indenter radius, sample height B set to 3 times the indenter radius.

R [μm]	H [μm]	H/R [-]	W [μm]	B [μm]
400	40	0.1	8000	1200
400	80	0.2	8000	2400
400	120	0.3	8000	3600
400	160	0.4	8000	4800

Table 1 (b): (R,H) case studies and respective model geometries for the evaluation of size dependence (constant equivalent deformation). Sample radius W set to 20 times the indenter radius, sample height B set to 3 times the indenter radius.

R [μm]	H [μm]	H/R [-]	W [μm]	B [μm]
400	40	0.1	8000	1200
125	12.5	0.1	2500	375
25	2.5	0.1	500	75
7.5	0.75	0.1	150	22.5

In Table 2, the results obtained from the sensitivity analyses with respect to geometrical parameters are summarized. The real component of the indentation modulus in drained condition $\left(E'^*(0) \right)$ and that in the undrained solution $\left(E'^*(f \to \infty) \right)$ have been obtained through the finite element model and using equation (28) with $f = 0$ and $f = 10^7$, respectively. The maximum $tan(\phi_f)$ has been obtained by sweeping the frequency domain and selecting the maximum value of $tan(\phi_f) = \frac{E''^*(f)}{E'^*(f)}$.

A good consistence is found in terms of reduced storage modulus E'^* and reduced loss modulus E''^* computed at limit conditions. Using equation (17.a), one has the analytical estimates $E'^*(0) = 387$ kPa and $E'^*(f \to \infty) = 652$ kPa. Results in Table 2 fit well, bearing in mind that the undrained stiffness matrix can be defined only asymptotically.

In Figure 3 the values of $\overline{E'^*}$ (consolidation ratio) are presented for both constant radius (a) and constant H/R ratio (b) cases, versus frequency. For both sets of analy-

Table 2: Geometric sensitivity analysis, involving all case studies.

CASE STUDY [**R − H**]	E'*(0) [kPa]	E'* (**f → ∞**) [kPa]	$\frac{E'^*(0)}{E'^*(f\to\infty)}$ [numerical]	Max $\tan(\phi_\mathbf{f})$	f_{max}[**Hz**]	$\frac{E'^*(0)}{E'^*(f\to\infty)}$ [analytical]
400-160	354	520	0.68	0.1111	0.0129	0.6
400-120	359	535	0.67	0.1158	0.0129	
400-80	372	561	0.66	0.1214	0.0245	
400-40	394	604	0.65	0.1287	0.0468	
125-12.5	394	604	0.65	0.1287[1]	0.468	
25-2.5	394	604	0.65	0.1287	12	
7.5-0.75	394	602	0.65	0.1287	124	

ses, it has been found that the frequency response shifts towards higher frequencies at decreasing penetration depth (Figure 3.a) or decreasing indenter radius (Figure 3.b).
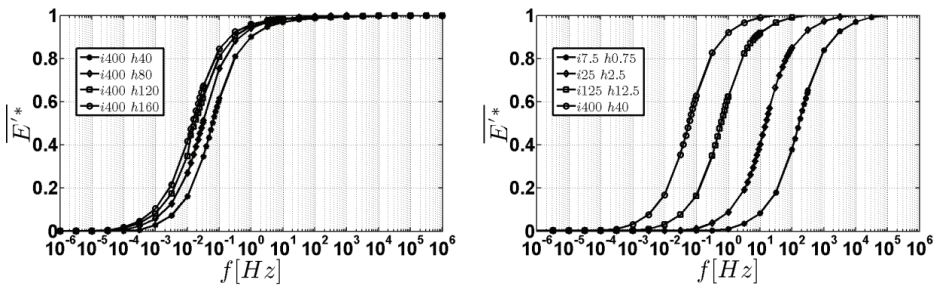

Figure 3: (a) $\overline{E'^*}$ vs frequency for the simulations at given radius (left) and (b) simulations at given ratio (right).

Figures 4.a and 4.b, show that the frequency responses overlap for all numerical experiments when normalized frequency (equation 30) is used.

Figure 5 shows the tangent of the phase shift for all the analyzed cases. A shift of the frequency at peak can be found for both sets of numerical examples.

As for the consolidation rate, the response in terms of tangent of phase shift versus normalized frequency shows an overlap of frequency at peak (Figure 6). It is worth noting that the geometric parameters *R* and *H* affect the frequency at peak in both sets of analyses.

The relationship between the frequency at peak versus the geometrical parameter
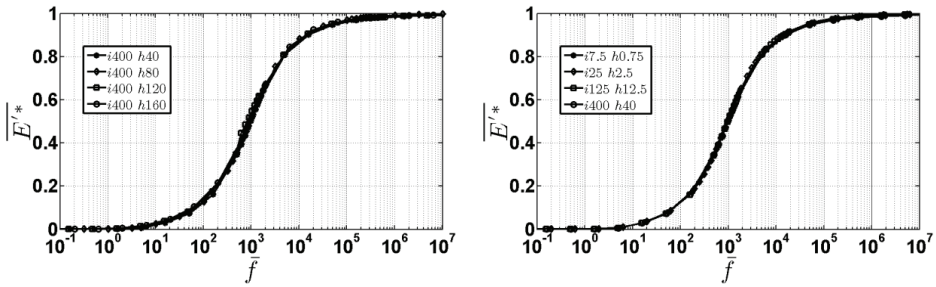
Figure 4: (a) $\overline{E'^*}$ vs normalized frequency for the simulations at given radius (left) and (b) simulations at given ratio (right).
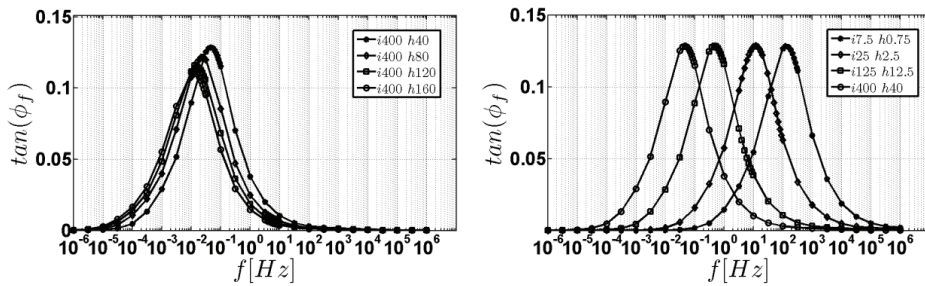

Figure 5: (a) $tan(\phi_f)$ vs frequency for the simulations at given radius (right) and (b) simulations at given ratio (left).
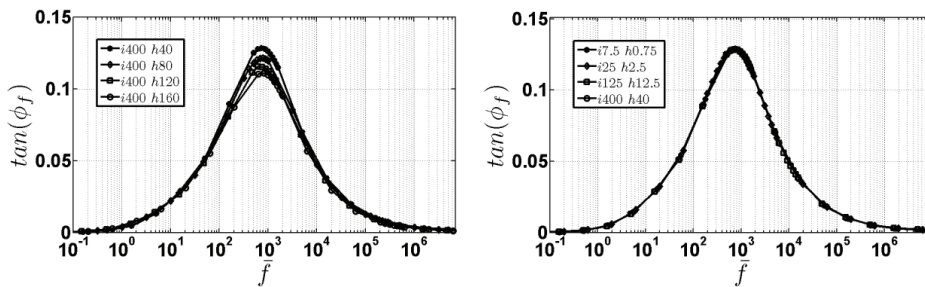

Figure 6: (a) $tan(\phi_f)$ vs normalized frequency for the simulations at given radius (left) and (b) simulations at given ratio (right).

RH, in a log-log plot, is presented in Figure 7; a good fitting with a linear function has been found of equation: $f_{max} = 711.52(RH)^{-0.996}$
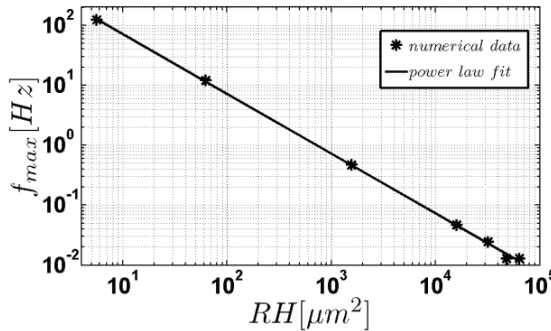

Figure 7: f_{max} vs geometrical parameter (RH) for all cases.

4.2   *Effect of constitutive parameters*

For sake of brevity the parameters used to define the anisotropic material behavior are described in Appendix A; in particular, the transversely isotropic model is presented.

The sensitivity analysis is performed here with respect to the anisotropy ratio λ and the out-of-plane Poisson's ratio v. The other constitutive parameters (G, E_a, η) are kept fixed according to the following assumptions:

- Shear modulus has been assumed as $G = 100$ KPa;

- axial Young modulus has been chosen according to the following relationship $E_a = 2G$;

- two different cases have been considered for the in-plane Poisson's ratio η: a) $\eta = 0$ and b) $\eta = v$.

In Tables 3 and 4 the values of parameters λ and v used in the analyses are presented, for in-plane Poisson's ratio $\eta = 0$ and $\eta = v$, respectively.

As shown in Appendix A, for a fixed set of parameters (G, E_a, λ, η), an upper bound for the out-of-plane Poisson's ratio v, namely v_{max}, can be found. The results, for each value of the anisotropy ratio λ, are presented here for different values of $\frac{v}{v_{max}}$.

Table 3: Parametric study in the case of in-plane Poisson's ratio $\eta = 0$.

λ		1	0.8	0.6	0.4	0.2	0.1
v/v_{max}	0.2	0.141	0.127	0.110	0.090	0.063	0.045
	0.4	0.283	0.253	0.219	0.179	0.126	0.089
	0.6	0.422	0.375	0.329	0.268	0.190	0.134
	0.8	0.566	0.506	0.438	0.358	0.253	0.179
	0.9	0.636	0.569	0.493	0.403	0.285	0.201

Table 4: Parametric study in the case of in-plane Poisson's ratio $\eta = v$.

λ		1	0.8	0.6	0.4	0.2	0.1
v/v_{max}	0.2	0.1	0.093	0.084	0.072	0.054	0.04
	0.4	0.2	0.185	0.167	0.143	0.108	0.08
	0.6	0.3	0.278	0.251	0.215	0.162	0.12
	0.8	0.4	0.371	0.334	0.287	0.216	0.16
	0.9	0.45	0.417	0.376	0.326	0.243	0.18

The drained to undrained ratio $\frac{E'^*(0)}{E'^*(f \to \infty)}$ obtained through the numerical model is reported as a function of α and for in-plane Poisson's ratio $\eta = 0$ (Figure 8.a); a good agreement with the analytical estimation is also observed (dashed lines). In Figure 8.b a comparison between the two cases a) $\eta = 0$ and b) $\eta = v$ is reported. In all cases a decrease of the drained to undrained ratio is found for materials with high anisotropy ratio (small λ). It is worth noting that the drained to undrained ratio can be smaller than 0.5 (lower bound for isotropic materials) for λ smaller than 0.4.
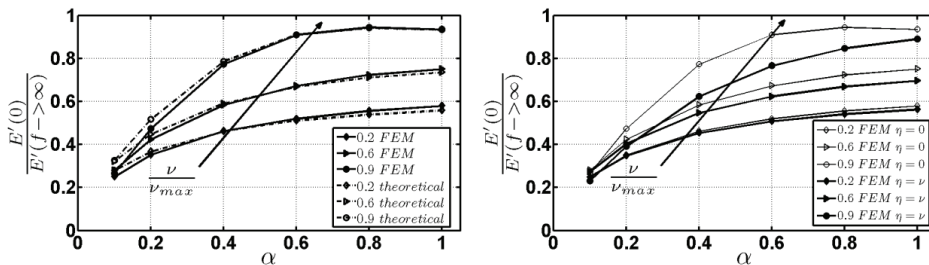

Figure 8: (a) The drained to undrained ($\frac{E'^*(0)}{E'^*(f \to \infty)}$) vs α is shown, parametrized with the ratio v/v_{max}. Solid lines refer to FEM simulations; dotted lines refer to analytical solutions (left). (b) Comparison of the drained to undrained ratio for $\eta = 0$ (open symbols) and $\eta = v$ (filled symbols) (right).

In Figure 9, the tangent of the phase shift as a function of α is presented, showing the comparison between the two cases of in-plane Poisson's ratio η. Figure 9 shows that the peak of phase shift is significantly affected by the anisotropy ratio; whereas, the frequency at peak is affected by the anisotropy ratio to a lesser extent.
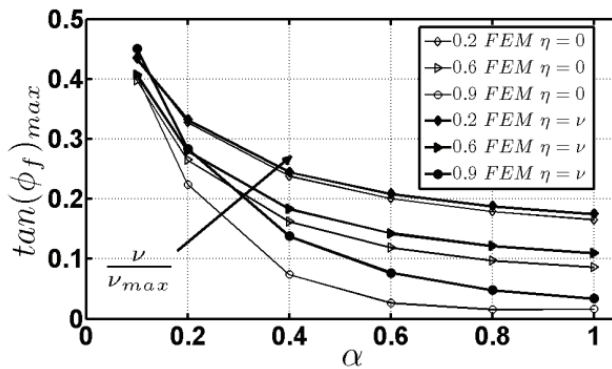

Figure 9: $Tan(\emptyset_f)$ vs α parametric with the ratio $\frac{v}{v_{max}}$; $\eta = 0$ (open symbols) $\eta = v$ (filled symbols).

Indeed, Figure 10 shows a decrease of the frequency at peak while remaining within the same order of magnitude; the case $\eta = v$ is shown.
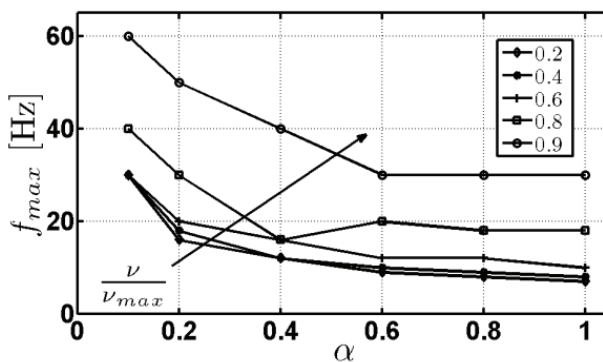

Figure 10: f_{max} vs α parametric with the ratio $\frac{v}{v_{max}}$.

5 Discussion and conclusions

The object of this study was to assess the frequency response of hydrated biological tissues to dynamic indentation loading through a numerical approach. The focus was on the effects of the characteristic lengths of the experiment and of the anisotropic properties of the tissue.

The results have shown that the indentation radius (for constant penetration depth) has a large effect on the real part of the material response (see Figure 3.a), whereas penetration depth (for constant *H/R* ratio, namely for constant equivalent deformation) has a negligible effect on the real part of the response (see Figure 3.b). In both cases, we have shown that, when normalized (dimensionless) frequency is used, the geometric effect disappears (all curves overlaps). This is consistent with a purely poroelastic response of the material as can be inferred from the analytical solution presented for the one dimensional confined compression in the frequency domain. Indeed, the analytical solution shows that the frequency response of pressure (31a,b) is dependent on the ratio $\frac{fL^2}{c}$ thus indicating that a the problem is strictly dependent on a dimensionless frequency $\overline{f} = \frac{fL^2}{c}$ in which the characteristic length of the experiment (*L*) is introduced. In this work we have extended this concept to the frequency domain by introducing the dimensionelss frequency for the indentation problem (Equation 30).

In the case of constant tip radius, if the indentation depth grows, both the values of $E'^*(0)$ and $E'^*(f \rightarrow \infty)$ decrease, as well as the maximum value of the tangent of the phase shift. For a large indentation depth, that is still reasonable in real experiments, the ratio $\frac{E'^*(0)}{E'^*(f \rightarrow \infty)}$ is higher and both $E'^*(0)$ and $E'^*(f \rightarrow \infty)$ are lower than expected from theory (see Table 2): the assumption of Hertzian contact introduced in the work of Delafargue and Ulm (2004) may then not hold.

A good agreement between numerical and analytical responses in terms of the real part ($\frac{E'^*(0)}{E'^*(f \rightarrow \infty)}$) has been found for anisotropic poroelastic material. Slight differences found between numerical and analytical predictions can be due to the limitations of the elastic contact solutions used in the analytical model.

Furthermore, the undrained to drained ratio is strongly dependent on the anisotropy ratio. In fact, the lowest values of $\frac{E'^*(0)}{E'^*(f \rightarrow \infty)}$ can be found for strongly anisotropic materials, i.e. $\lambda \ll 1$, while for isotropic material $\frac{E'^*(0)}{E'^*(f \rightarrow \infty)} > 0.5$.

By combining the information on Figures 8.b and 9, it is possible to infer that for a small anisotropy ratio $\lambda \ll 1$, both the undrained to drained $\frac{E'^*(0)}{E'^*(f \rightarrow \infty)}$ ratio and the tangent of the phase are less sensitive to Poisson coefficients. This is an advantage when identifying material properties of anisotropic materials for which it is difficult to identify Poisson's ratios accurately. Even if the sensitivity analysis is

performed on a relatively small range of variability for some parameters (e.g. the in-plane Poisson's ratio η), the results show that the mechanical properties can vary to a large extent in some regions of the space defined by the 5-ple $(G, E_a, \lambda, \eta, \nu)$ for a transversely isotropic material. Other works have already shown that dynamic indentation testing on cartilage tissue is a technique able to provide more information with respect to quasi-static indentation experiments [Miller and Morgan (2010); Han, Frank, Greene, Lee, Hung, Grodzinsky and Ortiz (2011)].

The results obtained in the present work lead to two important conclusions: first, if poroelasticity is the main dissipation mechanism for tissues exhibiting a time dependent response under dynamic indentation, then the results in terms of the dimensionless frequency (Equation 30) will be independent on the geometric parameters. Consequently, if further size dependence is still observed in the dimensionless frequency domain, then further dissipative mechanisms are playing a role, and viscoelasticity would probably be involved. A second relevant result obtained in the present investigation is that nanoindentation experiments on poroelastic specimens in the frequency domain are strongly affected by material anisotropy. It follows that anisotropy ratio of anisotropic tissues (like articular cartilage) can be identified by carrying out nanoindentation experiments along one single direction in the frequency domain. In this case, experiments in drained and undrained conditions should be carried out.

Another topic which is worth of further investigation is the effect of adsorbed water. The theory presented in this paper is not able to explicitly account for water molecules which are not free to flow through the porous matrix. This water may have a relevant effect on drained properties of the tissue.

Further developments are required for a reliable application to the frequency dependent characterization of biological tissues like cartilage, such as the implementation of the anisotropy of the hydraulic tensor in the finite deformation framework like in [Athesian and Weiss (2010)] or in [Federico and Herzog (2008)], and the formulation of the frequency domain response of nonlinear fibril reinforced constitutive law, more suited for cartilage tissues. A continuous distribution of fibril orientation of the collagen network as proposed in [Shirazi, Vena, Sah, Klisch (2011)] or in [Federico and Gasser (2010)]. This latter improvement would imply the linearization of the finite strain nonlinear constitutive law to be used in place of the transversely isotropic linear equations which relates the increments of the stress with the increments of strains.

Appendix A. Transversely isotropic linear elastic material model

The constitutive relation in a transversely isotropic linear elastic material for an axi-symmetric framework yields:

$$
\begin{cases}
\varepsilon_r = \frac{\sigma_r}{E_1} - \frac{v_2 \sigma_z}{E_2} - \frac{v_1 \sigma_\theta}{E_1} \\
\varepsilon_z = -\frac{v_2 \sigma_r}{E_2} + \frac{\sigma_z}{E_2} - \frac{v_2 \sigma_\theta}{E_2} \\
\varepsilon_\theta = -\frac{v_1 \sigma_r}{E_1} - \frac{v_2 \sigma_z}{E_2} + \frac{\sigma_\theta}{E_1} \\
\gamma_{rz} = \frac{\tau_{rz}}{G_2}
\end{cases}
\tag{A.1}
$$

where r, z and θ are respectively the axial, radial and circumferential coordinates. The subscripts 1 and 2 indicate the 'in-plane' contribution (radial and circumferential directions) and the 'out-of-plane' contribution (axial direction), respectively; in the r-θ plane the material response isotropic.

Defining the anisotropy ratio $\lambda = \frac{E_2}{E_1}$ and recalling $E_2 = E_a$, $v_2 = v$ and $v_1 = \lambda \eta$, the compliance matrix can be written as

$$
\mathbf{D} = \frac{1}{E_a}
\begin{bmatrix}
\lambda & -v & -\lambda \eta & 0 \\
-v & 1 & -v & 0 \\
-\lambda \eta & -v & \lambda & 0 \\
0 & 0 & 0 & \frac{E_a}{G_2}
\end{bmatrix}
\tag{A.2}
$$

The validity of the constitutive relation, in a thermodynamic sense, is subjected to the positive definition of the compliance matrix. Because of the symmetry of the matrix, the conditions come from the positivity of principal minors, as follows:

$$
\begin{cases}
\lambda > 0 \\
-\sqrt[2]{\lambda} < v < +\sqrt[2]{\lambda} \\
-\frac{\sqrt[2]{2} * \sqrt[2]{\lambda - \lambda \eta}}{2} < v < +\frac{\sqrt[2]{2} * \sqrt[2]{\lambda - \lambda \eta}}{2}
\end{cases}
\tag{A.3}
$$

As shown Figure A.1, given a value of η, v can span over the space defined under the respective thin curve, because the more restrictive condition is given by the third Equation in system (A.3).

If one considers the case in which the in plane and the out-of-plane Poisson's ratios are equal, the compliance matrix becomes

$$
\mathbf{D} = \frac{1}{E_a} *
\begin{bmatrix}
\lambda & -v & -\lambda v & 0 \\
-v & 1 & -v & 0 \\
-\lambda v & -v & \lambda & 0 \\
0 & 0 & 0 & \frac{E_a}{G_2}
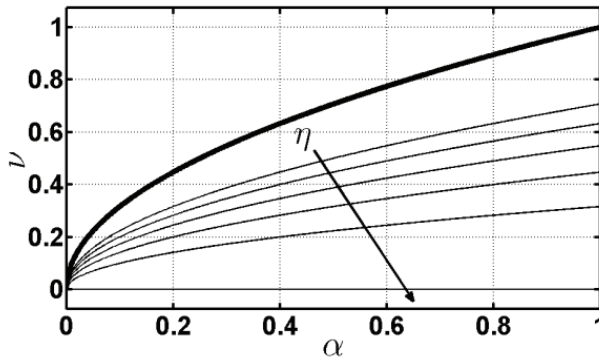\end{bmatrix}
\tag{A.4}
$$

Figure A.1: Bold line: plot of (A.3.2); thin lines: plot of (A.3.3), assuming η as parameter. Only positive values of v are considered.
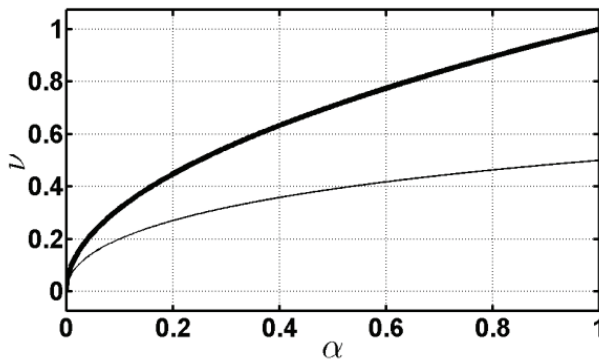

Figure A.2: Bold line: plot of (A.5.2); the solid line is the graph of the third equation in (A.5.3). Only positive values of v are considered.

and the positively definiteness conditions have the form of

$$
\begin{cases}
\lambda > 0 \\
-\sqrt[2]{\lambda} < v < +\sqrt[2]{\lambda} \\
-\frac{\lambda}{4} - \frac{\sqrt[2]{\lambda^2+8\lambda}}{4} < v < -\frac{\lambda}{4} + \frac{\sqrt[2]{\lambda^2+8\lambda}}{4}
\end{cases}
\tag{A.5}
$$

In Figure A.2 as well, given a value of η, v can span over the space defined under the thin curve, because the more restrictive condition is given by the third equation in system (A.5).

6 References

Almeida, E.S.; Spilker, R.L.(1998): Finite element formulations for hyperelastic transversely isotropic biphasic soft tissues. *Computer Methods in Applied Mechanics and Engineering*, vol. 151, pp.513-538.

Armstrong, C.G.; Lai, W.M.; Mow, V.C.(1984): An analysis of the unconfined compression of articular cartilage. *Journal of Biomedical Engineering*, vol. 106, pp. 165-173.

Athesian, G.A.; Weiss, J.A. (2010): Anisotropic hydraulic permeability under finite deformation. *Journal of Biomechanical Engineering*, vol. 132, pp. 111004-1:7.

Biot, M.A.(1941):General theory of three dimensional consolidation. *Journal of Applied Physics*, vol. 12, pp. 155-164.

Boschetti, F.; Pennati, G.; Gervaso, F.; Peretti, G.M.; Dubini, G. (2004): Biomechanical properties of human articular cartilage under compressive loads. *Biorheology*, vol. 41, pp. 159-166.

Buckwalter, J.A.; Mankin, H.J.(1997): Articular Cartilage. *The Journal of Bone and Joint Surgery*, vol. 79, pp. 600-611.

Chandran, P.L.; Barocas, V.H. (2006): Affine versus non-affine fibril kinematics in collagen networks: theoretical studies of network behavior. *ASME Journal of Biomechanic Engineering*, vol. 128, pp. 259-270.

Cheng, Y.T.; Ni, W.; Cheng, C.M.(2006): Nonlinear analysis of oscillatory indentation in elastic and viscoelastic solids. *Physical Review Letters*, vol. 97.

Cowin, S.C.; Doty, S.B.(2006): *Tissue Mechanics*. Springer Verlag, New York.

Delafargue, A.; Ulm, F.J. (2004): Explicit approximations of the indentation modulus of elastically orthotropic solids for conical indenters. *International Journal of Solids and Structures*, vol. 41, pp. 7351-7360.

Ebenstein, D.M.;Pruitt, L.A.(2006): Nanoindentation of biological materials. *Nano Today*, vol. 1, pp. 26-33.

Federico, S.; Gasser, T.C.(2010): Nonlinear elasticity of biological tissues with statistical fibre orientation. *Journal of the Royal Society Interface*, vol. 7, pp. 955-966.

Federico, S.; Herzog, W.(2008): On the anisotropy and inhomogeneity of perme-

ability in articular cartilage. *Biomechanics and Modeling in Mechanobiology*, vol. 7, pp. 367–378.

Fratzl, P. (2008): *Collagen – Structure and Mechanics*. Springer, Berlin.

Galli, M.; Oyen, M.L. (2009): Fast Identification of Poroelastic Parameters from Indentation Tests. *CMES: Computer Methods in Engineering and Sciences*, vol. 48.

Gouldstone, A.; Chollacoop, N.; Dao, M.; Li, J.; Minor, A.M.; Shen, Y.L.(2007): Indentation across size scales and disciplines: recent developments in experimentation and modeling. *Acta Materialia*,vol. 55, pp. 4015-4039.

Han, L.; Frank, E.H.; Greene, J.J.; Lee, H.Y.; Hung, H.H.K.; Grodzinsky, A.J.; Ortiz, C. (2011): Time-dependent nanomechanics of cartilage. *Biophysical Journal*, vol. 100, pp. 1846-1854.

Hu, Y.; Chen, X.; Whitesides, G.M.; Vlassak, J.J.; Suo, Z. (2011): Indentation of polydimethylsiloxane submerged in organic solvents. *Journal of Material Research*, vol. 26, pp. 785-795.

Hu, Y., Zhao, X.; Vlassak, J.J.; Suo, Z.(2010): Using indentation to characterize the poroelasticity of gels. *Applied physics and letters*, vol. 96, pp.121904-1:3.

Huang, C.Y.; Stankiewicz, A.; Athesian, G.A.; Mow, V.C. (2005): Anisotropy, inhomogeneity, and tension-compression nonlinearity of human glenohumeral cartilage in finite deformation. *Journal of Biomechanics*, vol. 38, pp. 799-809.

Jurvelin, J.S.; Buschmann, M.D.; Hunziker, E.B. (2003): Mechanical anisotropy of the human knee articular cartilage in compression. *Proc. Instn Mech. Engrs Part H: J. Engineering in Medicine*, vol. 217, pp. 215-219.

Karpfinger, F.; Muller, T.M.; Gurevich, B. (2009): Green's functions and radiation patterns in poroelastic solids revisited. *Geophysical Journal International*, vol. 178, pp. 327-337.

Kempson, G.E.; Muir, H.; Pollard, C.; Tuke, M.(1973): The tensile properties of cartilage of human femoral condyles related to the content of collagen and glycosaminoglycans. *Biochimica et Biophysica Acta - General Subjects*, vol. 297, pp. 456-472.

Kiviranta, P.; Lammentausta, E.; Töyräs, J.; Kiviranta, I.; Jurvelin, J.S. (2008): Indentation diagnostics of cartilage degeneration. *Osteoarthritis and Cartilage*, vol. 16, pp. 796-804.

Korhonen, R.K.; Laasanen, M.S.; Toyras, J.; Rieppo, J.; Hirvonen, J.; Helminen, H.J.; Jurvelin, J.S. (2002): Comparison of the equilibrium response of articular cartilage in unconfined compression, confined compression and indentation. *Journal of Biomechanics*, vol. 35, pp. 903-909.

Lu, X.L.; Wan, L.Q.; Guo, X.E.; Mow, V.C. (2010): A linearized formulation of triphasic mixture theory for articular cartilage and its application to indentation analysis. *Journal of Biomechanics*, vol. 43, pp. 673-679.

Maceri, F.; Marino M.; Vairo G. (2010): A unified multiscale mechanical model for soft collagenous tisues with regular fiber arrangement. *Journal of Biomechanics*, vol. 43, pp. 355-363.

Miller, G.J.; Morgan, E.F. (2010): Use of microindentation to characterize the mechanical properties of articular cartilage: comparison of biphasic material properties across length scales. *Osteoarthritis and Cartilage*, vol. 18, pp. 1051-1057.

Mow, V.C.; Kuei, S.C.; Lai, W.M.; Armstrong, C.G. (1980): Biphasic creep and stress relaxation of articular cartilage in compression - theory and experiment. *Journal of Biomechanical Engineering*, vol. 102, pp. 73-84.

Oyen, M.L.; Cook, R.F.(2009): A practical guide for analysis of nanoindentation data. *Journal of the mechanical behavior of biomedical materials*, vol. 2, pp. 396-407.

Shahsavari, R.; Ulm, F.J.(2009): Indentation analysis of fractional viscoelastic solids. *Journal of Mechanics of Materials and Structures*, vol. 4, pp. 523-550.

Shirazi, R.; Vena, P.; Sah, R.L.; Klish, S.M.(2011): Modeling the collagen fibril network of biological tissues as a nonlinear elastic material using a continuous volume fraction distribution function. *Mathematics and Mechanics of Solids*, vol.16, pp. 706-715.

Simha, N.K.; Jin, H.; Hall, M.L.; Chiravarambath, S.; Lewis, J.L.(2007): Effect of indenter size on elastic modulus of cartilage measured by indentation. *Journal of Biomechanical Engineering*, vol. 129, pp. 767-775.

Simon, B.R.(1992): Multiphase poroelastic finite element models for soft tissue structures. *Applied Mechanics Reviews*, vol. 45, pp. 191-218.

Spirt, A.A.; Mak, A.F.; Wassel, R.P. (1989): Nonlinear viscoelastic properties of articular cartilage in shear. *Journal of Orthopaedic Research*, vol. 7, pp. 43-49.

Tang H.; Buehler M.J.; Moran B. (2009):A constitutive model of soft tissue: from nanoscale collagen to tissue continuum. *Annals of Biomedical Engineering*, vol.37, pp. 1117-1130.

Terzaghi, V.(1943): *Thoretical soil mechanics*. Wiley, New York.

Vandamme, M.; Ulm, F.J. (2006): Viscoelastic solution for conical indentation. *International journal of Solid and Structures*, vol. 43, pp. 3142-3165.

Vlassak, J.J.; Ciavarella, M.; Barber, J.R.; Wang, X. (2003): The indentation modulus of elastically anisotropic materials for indenter of arbitrary shape. *Journal of Mechanics and Physics of Solids*, vol. 51, pp. 1701-1721.

Wilson, W.C.;van Donkelaar, R.; van Rietbergen, R.; Huiskes, R. (2007): The role of computational models in the search for the mechanical behavior and damage mechanisms of articular cartilage. *Medical Engineering and Physics*, vol. 27, pp. 810-826.